frontiers | Frontiers in Chemistry

TYPE Original Research
PUBLISHED 05 November 2024
DOI 10.3389/fchem.2024.1480356

OPEN ACCESS

EDITED BY
Haejin Hwang,
Inha University, Republic of Korea

REVIEWED BY
Jinwoo Park,
University of Seoul, Republic of Korea
Bolong Huang,
Hong Kong Polytechnic University, Hong Kong SAR, China

*CORRESPONDENCE
Seung Yong Lee,
lsy549@yonsei.ac.kr
Kyu Hyoung Lee,
khlee2018@yonsei.ac.kr

†These authors have contributed equally to this work

RECEIVED 13 August 2024
ACCEPTED 14 October 2024
PUBLISHED 05 November 2024

CITATION
Lee JH, Kang SH, Park GH, Kim MY, Ji S, Choa HE, Han GH, Hwang JY, Lee SY and Lee KH (2024) Emerging NO_2 gas sensing on substitutionally doped Fe on $NiWO_4$ SCES insulators.
Front. Chem. 12:1480356.
doi: 10.3389/fchem.2024.1480356

Emerging NO_2 gas sensing on substitutionally doped Fe on $NiWO_4$ SCES insulators

Jong Hyun Lee[1], Se Hwang Kang[2], Gi Hyun Park[1†], Min Young Kim[1†], Sanghyun Ji[1†], Ha Eun Choa[1], Gi Hyeon Han[1], Jeong Yun Hwang[1], Seung Yong Lee[1*] and Kyu Hyoung Lee[1,3*]

[1]Department of Materials Science and Engineering, Yonsei University, Seoul, Republic of Korea, [2]Material Science and Chemical Engineering Center Industrial Convergence Engineering Group, Institute for Advanced Engineering, Yongin-si, Gyeonggi-do, Republic of Korea, [3]Yonsei-KIST Convergence Research Institute, Seoul, Republic of Korea

In this study, we demonstrate the emergence of NO_2 gas sensing capabilities in the typically non-active $NiWO_4$, a strongly correlated electron system (SCES), by introducing substitutional Fe at the Ni site. $NiWO_4$ typically exhibits strong Coulombic repulsion between Ni atoms, resulting in a large band gap of over 3.0 eV and insulating behavior. This correlated behavior is clearly reflected in the significant increase of band gap when considering the Hubbard *U* correction for the cations, bringing the theoretical value closer to the observed value. The single-phase $Fe_{0.5}Ni_{0.5}WO_4$ displays a notable shift in the $[NiO_6]$ symmetric vibration mode and an increase in magnetization. Additionally, theoretical calculations confirm the preservation of the wide band gap, with the Fe and O levels generated within the band gap. These findings indicate that Fe located in the Ni sites modulate Coulombic repulsion in $NiWO_4$ SCES insulators. Unlike the poor gas-sensing performance of intrinsic $NiWO_4$, $Fe_{0.5}Ni_{0.5}WO_4$ exhibits a significant NO_2 response (R_g/R_a) of 11 at 200°C than other gases and a limit of detection (LOD) of 46.4 ppb. This study provides a pathway for realizing gas-sensing performance in strongly correlated electron insulators with large band gaps through the introduction of dopant levels at the cation sites.

KEYWORDS

metal oxide, $NiWO_4$, gas sensor, NO_2 gas, SCES

1 Introduction

Strongly correlated electron systems (SCES) are characterized by Coulombic repulsion between neighboring cations within a crystal structure, leading to the development of exotic physical properties (Dagotto, 2005; Jacqueline et al., 2022; Zewei et al., 2018; Sami et al., 2022; Morosan et al., 2012; Bhargava et al., 2020; Watthaisong et al., 2019; Cesare et al., 2021; You et al., 2016; Park et al., 2020). One notable feature of SCES is the presence of a pseudo-band gap, often referred to as the Mott gap, which arises due to strong Coulombic repulsion between cations, as commonly observed in NiO. The size of this pseudo-band gap depends on the Hubbard parameter (*U*) for each cation, as indicated by theoretical calculations. Additionally, SCES typically exhibit magnetic ordering, often in the form of antiparallel spin alignment, with net magnetization being influenced by the Coulombic repulsion between magnetic cations. However, the higher activation energy for electrical transport in SCES insulators, which typically follows the polaronic hopping conduction

model, results in a strong insulating behavior, making these materials challenging for a wide range of applications. Consequently, inherited properties governed by Coulombic repulsion in SCES insulators have inspired various strategies aimed at modulating the interactions between cations.

Among the various strategies for tuning SCES properties, we focus on $NiWO_4$, which exhibits Coulombic repulsion between Ni cations similar to the Mott-insulator behavior observed in NiO (Han et al., 2024; Lee et al., 2024). Theoretical calculations show that a pseudo-gap develops as the U value increases, reaching nearly 6 eV of U_{Ni}, a value that aligns with the experimentally measured band gap obtained from UV-vis spectroscopy. Additionally, calculation results are supported by the neutron diffraction results of $NiWO_4$, confirming the antiparallel spin ordering between Ni cations (Prosnikov et al., 2017). However, $NiWO_4$ possesses a monoclinic crystal structure, which has lower symmetry compared to the cubic structure of NiO, and it includes tungsten as an additional component. This provides an extra degree of freedom for tailoring the correlation effects, making it a promising candidate for various applications. For instance, substituting vanadium (V) into the Ni sites, which reduces the Coulombic repulsion strength between cations, could enhance chemical adsorption sites, suggesting the potential of $NiWO_4$ for diverse catalytic applications (Suh et al., 2024).

The chemoresistive type of gas sensor exemplifies an intersectional application of physical and chemical properties (Wang et al., 2018; Kim et al., 2023; Dey, 2018; Choi et al., 2021; Yamazoe, 2005; Lee et al., 2023; Jin et al., 2022; Chen et al., 2013; Franco et al., 2022; Ji et al., 2019). For optimal performance, such a sensor must ensure high and monotonic adsorption of gas molecules at specific sites on the material surface. This adsorption leads to the development of surface depletion or accumulation layers due to the exchange of charge carriers between the analyte gases and the material surface. The type of gas molecules (whether reducing or oxidizing) and the conduction type of the material (n-type or p-type) influence the change in resistance after gas exposure. The resistance then returns to its initial value once the analyte gas molecules desorb from the material surface. To enhance gas sensing functionality, we substitutionally introduced Fe mixed with Ni into $NiWO_4$, which initially exhibited poor gas-sensing performance. The Fe cation level, positioned within the band gap and modulating the weaker Coulombic repulsion, resulted in improved NO_2 gas sensing and selectivity. These findings present a strategy for expanding the potential applications of SCES materials beyond gas sensing, which can be achieved by tailoring Coulombic repulsion.

2 Materials and methods

2.1 Material synthesis

The $NiWO_4$ and $Fe_{0.5}Ni_{0.5}WO_4$ powders were synthesized using a solid-state reaction. High-purity Fe_2O_3 (Kojundo Chemical Lab, 99.9%), NiO (Kojundo Chemical Lab, 99.97%), and WO_3 (Kojundo Chemical Lab, 99.9%) powders were mixed following the nominal atomic ratio of $NiWO_4$ and $Fe_{0.5}Ni_{0.5}WO_4$ in an alumina mortar with ethanol for wet mixing. The mixed powders underwent heat treatment in an electric box furnace at 900°C for 12 h. The crystal structure characterization of the synthesized powders was performed by X-ray diffraction (XRD, Smart Lab, Rigaku) with Cu Kα radiation and Raman spectroscopy (LabRAM ARAMIS, Horiba Jobin Yvon).

2.2 Theoretical calculation

The structural optimization and electronic structure calculations were performed using the density functional theory (DFT), as implemented in the QUANTUM-ESPRESSO (Sandro et al., 2005; Giannozzi et al., 2009; Giannozzi et al., 2017), using the Perdue–Burke–Ernzerhof (PBE) generalized-gradient approximation (GGA) functional (Perdew et al., 1996) and projector augmented wavefunction (PAW) pseudopotentials (Blöchl, 1994). Convergence tests on kinetic-energy cutoff and k-point density showed that the 120 Ry and 4 × 4 × 4 Monkhorst–Pack (Monkhorst and Pack, 1976) k-point grid are efficient and accurate enough. The crystal structure (materials project ID: mp-21179) was double along the a-axis to reflect that $NiWO_4$ has an antiferromagnetic order. The structure was then relaxed to the remaining force, and stress can be less than 10–3 Ry/Bohr and 0.1 kbar. These calculations were performed under the collinear spin-polarized scheme where the spin quantization axis was fixed to the Cartesian *z*-axis, which is only ~0.0131° off from the crystal c-axis. To consider the correlated nature of $NiWO_4$ appropriately, the Hubbard U repulsion parameters on Ni-3d, Fe-3d, and W-5d were added according to the scheme of Dudarev et al. (1998). Further relaxation of forces and stresses due to the inclusion of Hubbard U parameters were not performed. The Hubbard parameters were calculated self-consistently using the density functional perturbation theory (DFPT), as implemented in the HP code (Timrov et al., 2018; Timrov et al., 2021; Timrov et al., 2022).

2.3 Evaluation of the gas-sensing performance

A two-probe electrode configuration was employed for the gas-sensing analysis. $NiWO_4$ and $Fe_{0.5}Ni_{0.5}WO_4$ powders were put on the gold electrodes positioned on an alumina substrate with 0.2 mL of ethanol on synthesized powders, and the powder was physically pressed to fix the powder on the substrate. The gas-sensing performance of the fabricated sensors was evaluated within a custom-built chamber equipped with mass flow controllers, maintaining a fixed flow rate of 500 standard cubic centimeters per minute using air as the carrier gas. The sensors were exposed to the target gas concentrations increasing up to 20 ppm for 1,000 s, followed by a recovery period in the air for 500 s at room temperature, 100, and 200°C. The resistance values in air (R_a) and upon exposure to the target gases (R_g) were recorded, and the sensor response (R_g/R_a) was determined by calculating the ratio of the resistance values in ambient air to under the target gas exposure conditions. Gas-sensing measurements were performed for various gases, including NO_2, H_2S, SO_2, benzene, CO, ethanol, and acetone.

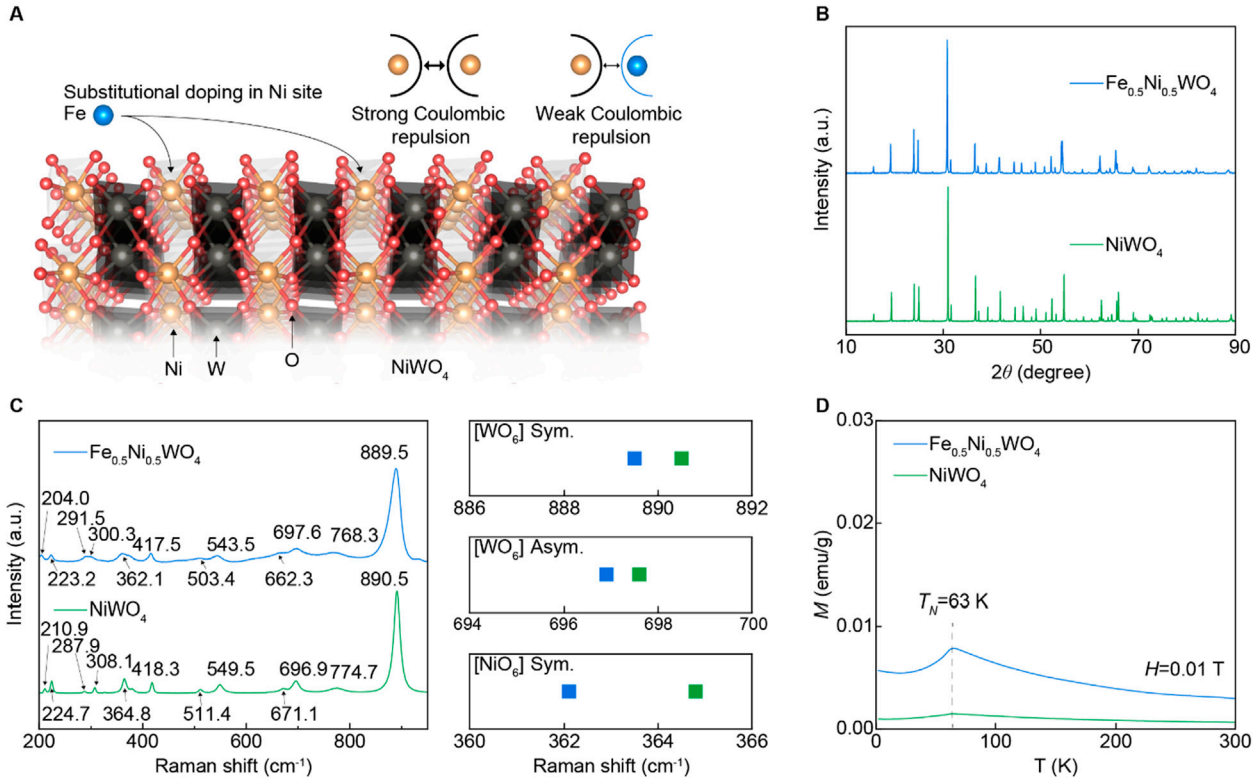

FIGURE 1
SCES insulator of $Fe_{0.5}Ni_{0.5}WO_4$. **(A)** Schematic strategy of Fe cations in the $NiWO_4$ crystal structure to modulate Coulombic repulsion. Difference in Coulombic repulsion between Ni–Ni and Ni–Fe. **(B)** XRD results of $NiWO_4$ and $Fe_{0.5}Ni_{0.5}WO_4$. **(C)** Raman spectroscopy results of $NiWO_4$ and $Fe_{0.5}Ni_{0.5}WO_4$. The plot on the right side is a description of the peak shifts for $[WO_3]$ symmetric, $[WO_3]$ asymmetric, and [NiO] symmetric vibration modes. **(D)** Temperature dependence magnetization curve under 0.01 T.

3 Results

3.1 Substitutionally located Fe in the Ni site for SCES $NiWO_4$

The $NiWO_4$ strongly correlated electron system (SCES) exhibits a wolframite-type crystal structure (space group P2/c), composed of corner-shared [NiO_6] and [WO_6] octahedral sublattices, with significant Coulombic repulsion between Ni atoms (Prosnikov et al., 2017; Han et al., 2024; Suh et al., 2024). To modulate the Coulombic repulsion, we replaced Fe cations into the Ni sites of $NiWO_4$ using a solid-state synthesis method, as depicted in Figure 1A. The Fe cations typically exhibit a +2 to +3 oxidation state and have an atomic radius of 1.26 Å, which is similar to that of Ni cations (1.26 Å; +2 to +3 oxidation state). In contrast, W cations have a larger atomic radius of 1.41 Å and an oxidation state of +5 to +6. The same wolframite-type structure of $FeWO_4$, which also consists of corner-shared [FeO_6] and [WO_6] octahedral sublattices with analogous Wyckoff positions (Maignan et al., 2022), suggests that the Fe cations are substitutionally located in the Ni sites of $NiWO_4$. Figure 1B shows that both the synthesized $NiWO_4$ and $Fe_{0.5}Ni_{0.5}WO_4$ powders exhibit a single phase. Raman spectroscopy results in Figure 1C reveal that these monoclinic structures display 36 distinct Raman vibrational modes, including 8 Ag and 10 Bg active modes. Notably, the $Fe_{0.5}Ni_{0.5}WO_4$ sample shows a downward shift in peak positions compared to $NiWO_4$, particularly in the Ni–O symmetric vibration mode within [NiO_6], which shifts from 364.8 cm^{-1} in $NiWO_4$ to 362.1 cm^{-1} in $Fe_{0.5}Ni_{0.5}WO_4$, indicating weaker Ni–O bonding. This peak shift is more pronounced than those observed in the W–O asymmetric vibration mode near 698 cm^{-1} and the W–O symmetric vibration mode near 890 cm^{-1}. The temperature-dependent magnetization (M) curve reveals a Néel temperature (T_N) of 63 K for both $NiWO_4$ and $Fe_{0.5}Ni_{0.5}WO_4$ compositions, with $Fe_{0.5}Ni_{0.5}WO_4$ exhibiting higher magnetization, as shown in Figure 1D, which suggests reduced Coulombic repulsion, which is common in SCES (Park et al., 2020). The XRD and Raman results confirm that Fe is located at the Ni site within the single phase of the $NiWO_4$ SCES matrix.

To investigate the effect of Fe substitution theoretically, we calculated the electronic structure of $NiWO_4$ and $Fe_{0.5}Ni_{0.5}WO_4$ SCES, whose crystal structures are shown in Figure 2A. As reported in many earlier works, the Hubbard U scheme can enhance the accuracy of the calculation, especially the band gap. We first assumed 6.0 eV of on-site Coulomb repulsion energy for both Ni 3*d* and W 5*d*. The density functional perturbation theory (DFPT) calculation of Hubbard parameters was then performed on this ground state using a gamma-only ***q***-point mesh. This DFPT calculation yielded U = 6.5951 eV for Ni-3*d* and 3.4487 eV for W 5*d*. A new ground state with U = 6.6 eV for Ni-3*d* and U = 3.4 eV for W-5*d* was calculated. We again performed the DFPT calculation

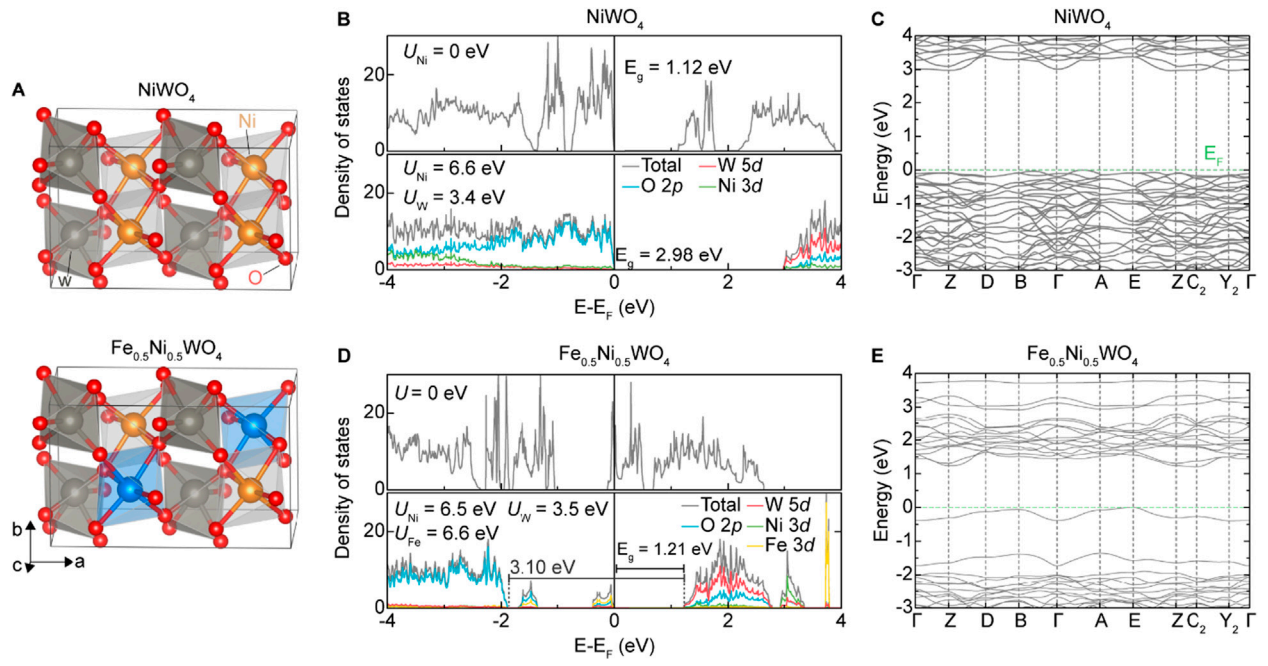

FIGURE 2
Theoretical results of $NiWO_4$ and $Fe_{0.5}Ni_{0.5}WO_4$ SCES. **(A)** Model structure of $NiWO_4$ (top) and $Fe_{0.5}Ni_{0.5}WO_4$ (bottom) from the DFT calculations. **(B, C)** Electronic structure of $NiWO_4$ of DOS (U = 0) and PDOS plots (U_{Ni} = 6.6 eV; U_W = 3.4 eV) **(B)** and band structure with the considered U value **(C)**. **(D, E)** Electronic structure of $Fe_{0.5}Ni_{0.5}WO_4$. The DOS and PDOS plot **(D)** and the band structure with the U value **(E)**.

TABLE 1 Calculated Hubbard parameters of each atom in eV. The values on the right in each cell of *U* represent the calculated Hubbard parameter when DFPT is applied to the ground state of the value on the left.

Iteration	U_{Ni}	U_{Fe}	U_W
$NiWO_4$			
1	6.0 | 6.5951	—	3.4 | 3.4487
2	6.6 | 6.5727	—	3.4 | 3.4571
2, q = 1 × 2 × 2	6.6 | 6.6125	—	3.4 | 3.4668
2, q = 2 × 4 × 4	6.6 | 6.6143	—	3.4 | 3.4669
$Fe_{0.5}Ni_{0.5}WO_4$			
1	6.9 | 6.3946	6.9 | 6.3772	3.5 | 3.4960
2	6.4 | 6.4320	6.4 | 6.4338	3.5 | 3.4718
2, q = 1 × 2 × 2	6.4 | 6.4731	6.4 | 6.5612	3.5 | 3.4865
2, q = 2 × 4 × 4	6.4 | 6.4740	6.4 | 6.5763	3.5 | 3.4875
3, q = 2 × 4 × 4	6.5 | 6.4651	6.6| 6.5522	3.5 | 3.4858

of Hubbard parameters, which resulted in quite converged values of U = 6.5727 eV for Ni-3*d* and U = 3.4561 eV for W-5*d*. Finally, we checked the dependency of the Hubbard parameters on the ***q***-point mesh size. The DFPT calculations of U on the ground state with U = 6.6 eV for Ni-3d and U = 3.4 eV for W-5*d* were performed using ***q***-point mesh of sizes of 1 × 2 × 2 and 2 × 4 × 4. As the ***q***-point size increases, U parameters also increase, but it does not vary much, showing a difference of U less than ~0.1 eV, as seen in Table 1, implying that the parameters are well-converged. The ground state with these self-consistently converged U parameters shows an indirect optical band gap of 2.98 eV, as shown in Figures 2B, C, which agrees well with some earlier results (Shepard and Smeu, 2018; Errandonea et al., 2023; Ye et al., 2023). We performed the same procedures to calculate the Hubbard parameters (Table 1), density of states (DOS), and the band structure of $Fe_{0.5}Ni_{0.5}WO_4$ (Figures 2D, E). We supposed identical U values for two Ni atoms

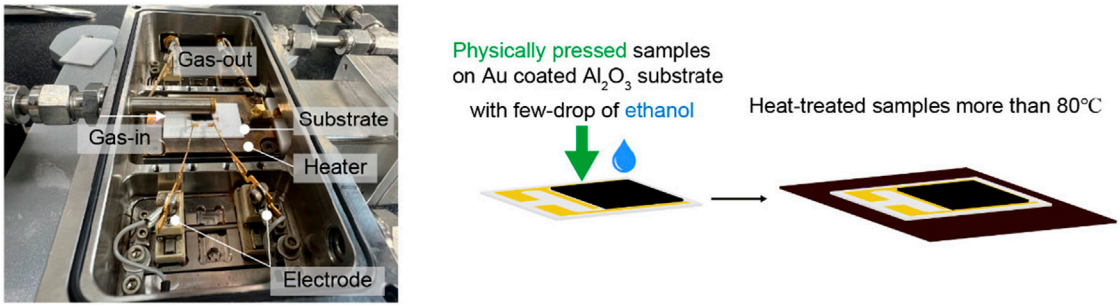

FIGURE 3
Photograph of the gas-sensing measurement system and the schematically described sampling methods.

and two Fe atoms due to their structural symmetry. The converged values slightly differ from the value of $NiWO_4$, but it rapidly converged, as iterated. The test for convergence on the ***q*** mesh revealed that the calculation with the gamma-point only has a small deviation. This deviation was reduced to less than 0.05 eV by an additional iteration. The correction with this converged *U* value modifies DOS remarkably, as shown in Figure 2D, showing that the system is strongly correlated. In addition, states mainly consisting of Fe-3*d* and O-2*p* appear near the Fermi energy. This contrasts that the states of $NiWO_4$ near the Fermi energy mainly consist of Ni-3*d* and O-2*p* (Errandonea et al., 2023). These observations imply the remarkable alteration of the conduction mechanism and characteristic in $Fe_{0.5}Ni_{0.5}WO_4$.

Summarizing the structure of $Fe_{0.5}Ni_{0.5}WO_4$ from the experimental and theoretical results above, it maintains the wolframite-type crystal structure while modulating the Coulombic repulsion between Ni atoms, as evidenced by the crystal structure distortion and enhanced magnetic properties compared to $NiWO_4$. Experimentally, the relatively higher Raman shift of the [NiO_6] symmetric vibration mode, compared to the [WO_6] vibration modes, indicates that Fe atoms preferentially occupy the Ni sites, leading to a distorted Ni–O bonding state. Additionally, the higher magnetization of $Fe_{0.5}Ni_{0.5}WO_4$, in contrast to the antiferromagnetic phase of $NiWO_4$, is attributed to the higher magnetic moment of Fe. Moreover, the presence of Fe states near the Fermi level (E_F) and within a 3.1-eV large depletion region, as suggested by the DFT results, indicates improved carrier transfer compared to $NiWO_4$. The following section demonstrates the emergence of gas-sensing performance in $Fe_{0.5}Ni_{0.5}WO_4$, in contrast to the lack of gas-sensing functionality in $NiWO_4$, as induced by the Fe dopant.

3.2 Emerging NO_2 gas sensing in $Fe_{0.5}Ni_{0.5}WO_4$

The gas-sensing measurements were conducted using a two-electrode system, as depicted in Figure 3. The samples were prepared by pressing the synthesized powder onto an Au-coated Al_2O_3 substrate, followed by the addition of a few drops of ethanol. The samples were then heat-treated to vaporize the ethanol and secure the material onto the substrate. The gas sensing tests were performed under a 20-ppm concentration of various gases, including NO_2, H_2S, H_2, SO_2, CO, benzene, ethanol, and acetone, at room temperature, 100°C, or 200°C. The results for NO_2 and H_2S gas responses from $Fe_{0.5}Ni_{0.5}WO_4$, shown in Figures 4A, B, indicate a significantly higher gas-sensing response at 200°C compared to that at RT and 100°C, highlighting this as the optimal operational temperature. A comparison of the gas-sensing responses between $NiWO_4$ and $Fe_{0.5}Ni_{0.5}WO_4$ reveals substantial differences in performance. For NO_2 detection, $Fe_{0.5}Ni_{0.5}WO_4$ exhibits a notable increase in resistance compared to the air environment, confirming that both $Fe_{0.5}Ni_{0.5}WO_4$ and $NiWO_4$ SCES function as p-type gas sensing materials. In contrast, $NiWO_4$ samples consistently demonstrated a low and nearly uniform response, with an absolute value of gas sensing response (R_g/R_a or R_a/R_g) close to 2 for all tested analyte gases, as shown in Figures 4A–H. However, $Fe_{0.5}Ni_{0.5}WO_4$ displayed a significantly enhanced gas-sensing response, with an R_g/R_a value of 10.4 under exposure to NO_2 gas, marking it as the highest response among the tested gases. The second highest response was under H_2S exposure, with a 2.8 response, which is still notably higher than the near 2 response observed for other gases such as H_2, SO_2, CO, benzene, ethanol, and acetone. The gas selectivity plot in Figure 4I further confirms the superior selectivity of $Fe_{0.5}Ni_{0.5}WO_4$ for NO_2. Figure 4J shows the comparison of NO_2 responses at various Fe concentrations measured at different temperatures, including room temperature (RT), 100°C, and 200°C. Although $Fe_{0.5}Ni_{0.5}WO_4$ exhibited a significant response of 11 at 200°C, $Fe_{0.25}Ni_{0.75}WO_4$ and $Fe_{0.4}Ni_{0.6}WO_4$ showed negligible gas-sensing responses across all measured temperatures. The higher gas-sensing performance of $Fe_{0.5}Ni_{0.5}WO_4$ highlights the optimized Fe concentration and operating temperature as critical combined factors that enhance adsorption and facilitate carrier transfer between the gas molecules and the surface.

Furthermore, the gas-sensing response to varying NO_2 concentrations is illustrated in Figures 5A, B. As the NO_2 concentration decreases from 20 ppm to 1 ppm, a corresponding decline in gas response is observed, which is particularly noticeable between the concentrations of 10 ppm and 1 ppm. However, the response saturated at 10 ppm and 20 ppm of NO_2, indicating a plateau in sensor performance at these levels. To further quantify the sensor's sensitivity, we calculated the LOD based on the responses at NO_2 concentrations of 10 ppm, 4 ppm, 2 ppm, and 1 ppm. From this analysis, an LOD of 46.4 ppb was determined. This value

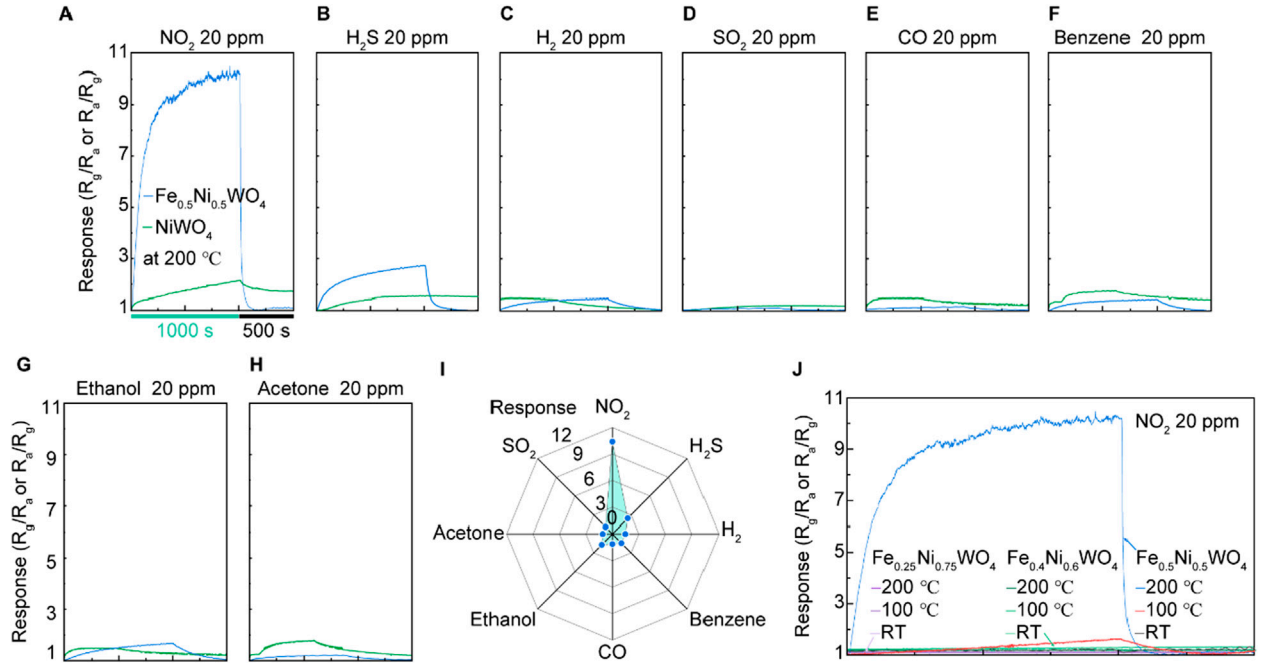

FIGURE 4
Gas-sensing results of $NiWO_4$ and $Fe_{0.5}Ni_{0.5}WO_4$ at 200°C under 20 ppm of different gases. **(A)** NO_2 at RT, 100°C, and 200°C, respectively. **(B)** H_2S at RT, 100°C, and 200°C. **(C)** H_2. **(D)** SO_2. **(E)** CO. **(F)** Benzene. **(G)** Ethanol. **(H)** Acetone. **(I)** Results of gas selectivity. **(J)** Comparison of the responses under an NO_2 environment and different temperatures using $Fe_{0.25}Ni_{0.75}WO_4$ and $Fe_{0.4}Ni_{0.6}WO_4$.

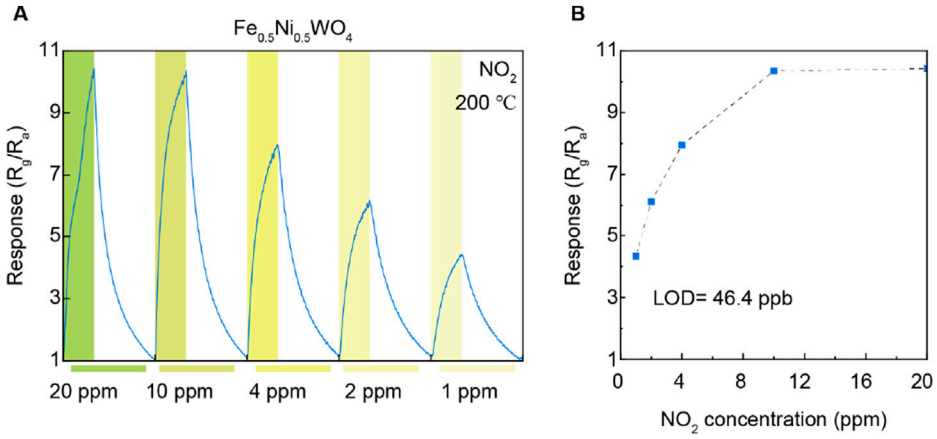

FIGURE 5
(A) Gas response under different NO_2 concentrations. **(B)** Limit of detection for NO_2 gases on $Fe_{0.5}Ni_{0.5}WO_4$.

underscores the sensor's capability to detect trace amounts of NO_2 with significant precision. The ability to achieve such a low LOD highlights the effectiveness of $Fe_{0.5}Ni_{0.5}WO_4$, which develops the material's gas-sensing performance, particularly at lower concentrations. These results underscore the effectiveness of Fe doping in $NiWO_4$, particularly in enhancing NO_2 gas-sensing performance at 200°C. The distinct difference in response between $NiWO_4$ and $Fe_{0.5}Ni_{0.5}WO_4$ highlights the critical role of Fe cations in modulating the gas-sensing properties, suggesting that the Fe dopant level could serve as an activating agent for the gas adsorption site and improved the charge carrier transfer for selective gas-sensing materials and various chemistry applications.

4 Conclusion

The Fe dopant level located at band gap is used for enhancing the gas-sensing functionality on the $NiWO_4$ SCES insulator, which shows negligible gas-sensitivity at 200°C for all measured gas molecules. The Coulombic repulsion between magnetic cations in

$NiWO_4$ open over 3.0 eV of the band gap, and dopant-level Fe is manipulated via being substitutionally located in the Ni site that developed 10.4 R_g/R_a under 20 ppm of an NO_2 environment. The Fe dopant implies playing an important role, such as activating the higher gas adsorption site or the higher carrier transferring from the charge carrier density changed between analyte gas molecules and materials' surface. These results encourage the use of further chemical sensing devices on SCES insulators by modulating the Coulombic repulsion between magnetic cations and dopant level-supporting at the Mott gap.

Data availability statement

The raw data in this manuscript will be available on request.

Author contributions

JL: Formal analysis, Methodology, Writing–review and editing. SK: Formal analysis, Methodology, Writing–review and editing. GP: Formal analysis, Investigation, Methodology, Writing–original draft. MK: Formal analysis, Investigation, Methodology, Writing–original draft. SJ: Methodology, Writing–original draft. HC: Data curation, Writing–original draft. GH: Data curation, Writing–original draft. JH: Methodology, Writing–original draft. SL: Conceptualization, Writing–original draft, Writing–review and editing. KL: Conceptualization, Writing–original draft, Writing–review and editing.

Funding

The author(s) declare that financial support was received for the research, authorship, and/or publication of this article. This research was supported by the Basic Science Research Program through the National Research Foundation of Korea (NRF) funded by the Ministry of Education NRF-2019R1A6A1A11055660 and 20013621. This research was also supported by a grant of the Korea Health Technology R&D Project through the Korea Health Industry Development Institute (KHIDI), funded by the Ministry of Health and Welfare, Republic of Korea, HI19C1234.

Conflict of interest

The authors declare that the research was conducted in the absence of any commercial or financial relationships that could be construed as a potential conflict of interest.

Publisher's note

References

Bhargava, A., Eppstein, R., Sun, J., Smeaton, M. A., Paik, H., Kourkoutis, L. F., et al. (2020). Breakdown of the small-polaron hopping model in higher-order spinels. *Adv. Mat.* 32, 2004490. doi:10.1002/adma.202004490

Blöchl, P. E. (1994). Projector augmented-wave method. *Phys. Rev. B* 50, 17953–17979. doi:10.1103/PhysRevB.50.17953

Cesare, F., Michele, R., Martin, S., and Ulrike, D. (2021). Polarons in materials. *Nat. Rev. Mat.* 6, 560–586. doi:10.1038/s41578-021-00289-w

Chen, X., Wong, C. K. Y., Yuan, C. A., and Zhang, G. (2013). Nanowire-based gas sensors. *Sens. Actuators B Chem.* 177, 178–195. doi:10.1016/j.snb.2012.10.134

Choi, M. S., Kim, M. Y., Mirzaei, A., Kim, H.-S., Kim, S.-I., Baek, S.-H., et al. (2021). Selective, sensitive, and stable NO_2 gas sensor based on porous ZnO nanosheets. *Appl. Surf. Sci.* 568, 150910. doi:10.1016/j.apsusc.2021.150910

Dagotto, E. (2005). Complexity in strongly correlated electronic systems. *Science* 309, 257–262. doi:10.1126/science.1107559

Dey, A. (2018). Semiconductor metal oxide gas sensors: a review. *Mat. Sci. Eng. B* 229, 206–217. doi:10.1016/j.mseb.2017.12.036

Dudarev, S. L., Botton, G. A., Savrasov, S. Y., Humphreys, C. J., and Sutton, A. P. (1998). Electron-energy-loss spectra and the structural stability of nickel oxide: an LSDA+U study. *Phys. Rev. B* 57, 1505–1509. doi:10.1103/PhysRevB.57.1505

Errandonea, D., Rodriguez, F., Vilaplana, R., Vie, D., Garg, S., Nayak, B., et al. (2023). Band-gap energy and electronic d–d transitions of $NiWO_4$ studied under high-pressure conditions. *J. Phys. Chem. C* 127, 15630–15640. doi:10.1021/acs.jpcc.3c03512

Franco, M. A., Conti, P. P., Andre, R. S., and Correa, D. S. (2022). A review on chemiresistive ZnO gas sensors. *Sens. Actuators Rep.* 4, 100100. doi:10.1016/j.snr.2022.100100

Giannozzi, P., Baroni, S., Bonini, N., Calandra, M., Car, R., Cavazzoni, C., et al. (2009). QUANTUM ESPRESSO: a modular and open-source software project for quantum simulations of materials. *J. Phys. Condens. Matter* 21, 395502. doi:10.1088/0953-8984/21/39/395502

Giannozzi, P., Baroni, S., Bonini, N., Calandra, M., Car, R., Cavazzoni, C., et al. (2017). Advanced capabilities for materials modelling with Quantum ESPRESSO. *J. Phys. Condens. Matter* 29, 465901. doi:10.1088/1361-648X/aa8f79

Han, G. H., Park, S. J., Park, G. H., Park, C. O., Lee, H., Lee, J. W., et al. (2024). Strongly correlated electron system $NiWO_4$: a new family of materials for triboelectrics using inherent Coulombic repulsion. *Nano Energy* 126, 109595. doi:10.1016/j.nanoen.2024.109595

Jacqueline, B., Andrea, C., Victor, G., Angel Hafezi, M. R., and Rubio, A. (2022). Strongly correlated electron–photon systems. *Nature* 606 (2022), 41–48. doi:10.1038/s41586-022-04726-w

Ji, H., Zeng, W., and Li, Y. (2019). Gas sensing mechanisms of metal oxide semiconductors: a focus review. *Nanoscale* 11, 22664–22684. doi:10.1039/C9NR07699A

Jin, C., Lim, J.-C., Kim, M. Y., Choi, M. S., Kim, S.-I., Baek, S.-H., et al. (2022). Impact of stirring time and the corresponding growth mechanism in the solvothermal synthesis of WO3 nanostructures. *J. Asian Ceram. Soc.* 10, 779–787. doi:10.1080/21870764.2022.2129483

Kim, M. Y., Lee, S. Y., Kim, J., Park, C. O., Shi, W., Min, H., et al. (2023). Generation of nanogaps on porous ZnO sheets via Li-ion implantation: NO_2 gas sensing with ultrafast recovery time. *Sens. Actuators B Chem.* 379, 133283. doi:10.1016/j.snb.2022.133283

Lee, M., Kim, M. Y., Kim, J., Park, C. O., Choa, H. E., Lee, S. Y., et al. (2023). Conductometric sensor for gaseous sulfur-mustard simulant by gold nanoparticles anchored on ZnO nanosheets prepared via microwave irradiation. *Sens. Actuators B Chem.* 386, 133726. doi:10.1016/j.snb.2023.133726

Lee, S. Y., Kim, I., Kim, H. J., Sim, S., Lee, J.-H., Yun, S., et al. (2024). A transparent p-type semiconductor designed via a polarizability-enhanced strongly correlated insulator oxide matrix. *Mater. Horiz. adv.* doi:10.1039/D4MH00985A

Maignan, A., Schmidt, M., Prots, Y., Lebedev, O. I., Daou, R., Chang, C.-F., et al. (2022). $FeWO_4$ single crystals: structure, oxidation states, and magnetic and transport properties. *Chem. Mat.* 34, 789–797. doi:10.1021/acs.chemmater.1c03640

Monkhorst, H. J., and Pack, J. D. (1976). Special points for Brillouin-zone integrations. *Phys. Rev. B* 13, 5188–5192. doi:10.1103/PhysRevB.13.5188

Morosan, E., Natelson, D., Nevidomskyy, A. H., and Si, Q. (2012). Strongly correlated materials. *Adv. Mater* 24, 4896–4923. doi:10.1002/adma.201202018

Park, S. G., Lee, K. H., Lee, J.-H., Bang, G., Kim, J., Park, H. J., et al. (2020). Improved polaronic transport under a strong Mott–Hubbard interaction in Cu-substituted NiO. *Inorg. Chem. Front.* 7, 853–858. doi:10.1039/C9QI01052A

Perdew, J. P., Burke, K., and Ernzerhof, M. (1996). Generalized gradient approximation made simple. *Phys. Rev. Lett.* 77, 3865–3868. doi:10.1103/PhysRevLett.77.3865

Prosnikov, M. A., Davydov, V.Yu., Smirnov, A. N., Volkov, M. P., Pisarev, R. V., Becker, P., et al. (2017). Lattice and spin dynamics in a low-symmetry antiferromagnet $NiWO_4$. *Phys. Rev. B* 96, 014428. doi:10.1103/PhysRevB.96.014428

Sami, D., Diego, A. Z., Alix, M., Franziska, W., Ross, M., Mathieu, T., et al. (2022). Control of electronic topology in a strongly correlated electron system. *Nat. Commun.* 13, 5729. doi:10.1038/s41467-022-33369-8

Sandro, S., Paolo, G., Carlo, C., Stefano, d. G., Alfredo, P., and Stefano, B. (2005). First-principles codes for computational crystallography in the Quantum-ESPRESSO package. *Z. Krist. - Cryst. Mat.* 220, 574–579. doi:10.1524/zkri.220.5.574.65062

Shepard, S., and Smeu, M. (2018). *Ab initio* study of structural and electronic properties of copper and nickel tungstate. *Comput. Mat. Sci.* 143, 301–307. doi:10.1016/j.commatsci.2017.11.021

Suh, J. W., Park, J., Jeong, S. H., Park, G. H., Choi, M. S., Jin, C., et al. (2024). Vanadium in strongly correlated electron system $Ni_{1-x}V_xWO_4$: paradoxically boosted $deNO_x$ reaction under SO_x environment via modulating electron correlation. *Appl. Catal. B Environ.* 343, 123540. doi:10.1016/j.apcatb.2023.123540

Timrov, I., Marzari, N., and Cococcioni, M. (2018). Hubbard parameters from density-functional perturbation theory. *Phys. Rev. B* 98, 085127. doi:10.1103/PhysRevB.98.085127

Timrov, I., Marzari, N., and Cococcioni, M. (2021). Self-consistent Hubbard parameters from density-functional perturbation theory in the ultrasoft and projector-augmented wave formulations. *Phys. Rev. B* 103, 045141. doi:10.1103/PhysRevB.103.045141

Timrov, I., Marzari, N., and Cococcioni, M. (2022). HP -- A code for the calculation of Hubbard parameters using density-functional perturbation theory. *Comput. Phys. Commun.* 279, 108455. doi:10.1016/j.cpc.2022.108455

Wang, H., Lustig, W. P., and Li, J. (2018). Sensing and capture of toxic and hazardous gases and vapors by metal–organic frameworks. *Chem. Soc. Rev.* 47, 4729–4756. doi:10.1039/C7CS00885F

Watthaisong, P., Jungthawan, S., Hirunsit, P., and Suthirakun, S. (2019). Transport properties of electron small polarons in a V_2O_5 cathode of Li-ion batteries: a computational study. *RSC Adv.* 9, 19483–19494. doi:10.1039/C9RA02923K

Yamazoe, N. (2005). Toward innovations of gas sensor technology. *Sens. Actuators B Chem.* 108 (1–2), 2–14. doi:10.1016/j.snb.2004.12.075

Ye, M., Zhou, Y., Shao, T., Liu, H., Tao, Q., Wang, X., et al. (2023). Effects of high pressure on the bandgap and the d–d crystal field transitions in wolframite $NiWO_4$. *J. Phys. Chem. C* 127, 6543–6551. doi:10.1021/acs.jpcc.2c09036

You, Z., Xiaofei, G., Hua, Z., Koushik, R., Suhare, A., Huaju, L., et al. (2016). Strongly correlated perovskite fuel cells. *Nature* 534, 231–234. doi:10.1038/nature17653

Zewei, S., Xun, C., Hongjie, L., and Ping, J. (2018). Recent progress in the phase-transition mechanism and modulation of vanadium dioxide materials. *NPG Asia Mat.* 10, 581–605. doi:10.1038/s41427-018-0061-2